

## An Improved Vat Photopolymerization Cure Model Demonstrates Photobleaching Effects

Mohammad Mahdi Emami<sup>1</sup> and David W. Rosen<sup>1,2</sup>

<sup>1</sup> Digital Manufacturing and Design Centre (DManD), Singapore University of Technology  
and Design, Singapore 487372, [mahdi\\_emami@sutd.edu.sg](mailto:mahdi_emami@sutd.edu.sg)

<sup>2</sup> George W. Woodruff School of Mech. Engineering, Georgia Institute of Technology,  
Atlanta, GA 30332, [david.rosen@me.gatech.edu](mailto:david.rosen@me.gatech.edu)

**Keywords:** Photopolymerization, Photobleaching, Grayscale Stereolithography, Volumetric Intensity

### Abstract

An improved high-fidelity simulation model for a grayscale projection micro-stereolithography process has been developed. The modeling purpose is to accurately predict cured part shapes and dimensions, given a radiation intensity distribution. The model employs COMSOL to solve a series of chemical reaction differential equations that model the evolution of chemical species (photoinitiator, monomer, and polymer) concentrations. Additionally, the model incorporates the effects of oxygen inhibition and species diffusion. This research offers two primary contributions to the cure model: the consideration of volumetric intensity to model variations in photoinitiator absorbance as a function of depth into the resin and a change to the rate model for photoinitiator to free radical conversion. The effects of these changes demonstrate observed photobleaching effects. Simulated cured part profiles are compared to experiments and demonstrate good agreement. Additionally, initial results are presented on the usage of the simulation model in a new process planning method.

### 1. Introduction

Monolayer photopolymerization with a grayscale mask can be used for fabrication of parts with a freeform surface profile in a single shot of exposure. Applications include micro-lens arrays and other optical components, as well as surface patterning with limited pattern height. Unlike layer-by-layer methods, the part is grown on a clear substrate by controlling the exposure energy distribution accordingly. However, obtaining such distribution that accurately cures desired profiles might be challenging and limits the accuracy regarding industrial application. Although the working curve is typically used in stereolithography processes, it only defines the relationship between exposure time and depth of cure [1,2]. However, for microfabrication of a freeform profile, lateral or side curing should be considered. This is the reason that expensive photoresists with long process times (layer deposition, prebaking, and development) are preferred for microfabrication [3,4]. Shrinkage and oxygen inhibition are limited by utilizing photoresists in comparison to liquid photopolymers.

Lateral curing or more precisely the prediction of a cured 3D profile is related to coupled factors and phenomena that occur during the irradiation process that makes modeling more complex. Some of these effects are oxygen inhibition, photo-bleaching, photo-trapping, self-focusing, and shrinkage [5]. All affected parameters and properties potentially can change the shape or dimensions of the final profile.

In one of the first attempts to cover the oxygen inhibition effect, Jariwala et. al. built a semi-empirical model of photochemical reactions with consideration of oxygen inhibition [6]. Then, they used this model to propose a process planning method for generating a series of binary masks to create spherical and aspherical lenses [7]. The simulation result demonstrated an overestimation discrepancy between COMSOL simulations and the experimental working curve for curing depths of more than 60  $\mu\text{m}$  [6].

Many researchers have studied and developed models for photobleaching (PB) effects. Depending on the nature of the photolysis products, the consumption of the photoinitiator can either lead to an increase in light intensity in the underlying layers (if the photolysis product is more transparent at the irradiating wavelengths) or a reduction in light intensity (if the photolysis product is strongly absorbing). Miller et. al. proposed a generalized model of PB for thick samples [8]. They conclude that diffusion is expected to have negligible effects in most PB systems. However, their work does not include experimental evidence.

This article builds on the foundation provided by researchers at Georgia Tech [6,7] to extend the photochemical model with a new differential equation for volumetric intensity to represent light intensity gradient as well as defining a new mechanism for initiator self-dissociation to incorporate the PB effect. Consequently, the proposed method can estimate the curing height for thick layers. The capability of this work has been demonstrated for the fabrication of microlens with sag heights of up to 800  $\mu\text{m}$ .

## 2. Chemical Kinematics of Photopolymerization

Free radical photopolymerization includes the stages of initiation, propagation, and termination, and the phenomena of species diffusion, heat generation, and oxygen inhibition [9]. The process starts with initiation when the photoinitiator molecule dissociates under UV radiation to form initiator radicals. Subsequently, the generated radical reacts with monomer species, producing primary radicals.

The process continues with the propagation step as monomer molecules react with the primary radical by a covalent bond and create an active polymer chain. The chain reaction continues until the termination step when radicals become extinguished or are otherwise unable to continue reacting. In the presence of dissolved oxygen, each active polymer chain or radical may react with oxygen to form a peroxide species, which converts them to an inactive polymer or dead radical. As a result, the propagation reaction is halted. The effect of oxygen inhibition described here is based on the works of Terrones-Pearlstein [10] and Dendukuri et. al. [11].

In contrast, our new modeling scheme includes one more step called “self-dissociation” of initiator to cover the PB effect. Simulations without this step correctly estimate the curing depth only for layers less than 350 $\mu\text{m}$  thick. Beyond this, the estimation error increases by depth. The PB effect was distinguished by Jacobs as the major reason for the observed super-logarithmic behavior of some photopolymer systems [12]. Comparing the simulated results of cure depth with the working curve obtained experimentally shows an underestimation of curing depth (refer Section 6, Figure 5.a).

In our photopolymer system (TMPTA and DMPA, see Section 5), the assumption is that the initiator is the only absorber of UV light. Also, a simple absorption test for pure TMPTA without initiator shows that it does not absorb UV light at 365nm. The initiators dissociate and consume

during the curing and so their concentration gradually reduced. So, the absorptivity of UV light changes over time of exposure and it allows more photons to penetrate and reduce the attenuation of light. This is called the photo-bleaching effect and is our primary hypothesis to explain the observed super-logarithmic behavior of our photopolymer

Simulation results without self-dissociation indicated that the consumption rate of initiator is not high enough to demonstrate a PB effect. It means that other mechanisms might exist for converting the initiator to molecule without UV absorption. Photolysis of DMPA (initiator) showed that various chemical reactions and products were observed, depending on the intensity level [13]. Furthermore, dissociation may occur by the heat energy produced by polymerization. To model these effects, a new self-dissociation reaction equation is added to our COMSOL model. The abovementioned chemical reactions are summarized in Table 1. The corresponding ordinary differential equations related to the dynamic concentration of the species are listed in Table 2.

Table 1 – List of main chemical reactions occurred during photopolymerization

Chemical Formula	Description of reactions	Product
$I \xrightarrow{K_d} 2R^*$	Photoinitiator Dissociation	Free Radical
$I + R^* \xrightarrow{K_{self}} I_{dead} + R^*$	Self-Dissociation	Dead Radical
$R^* + M \xrightarrow{K_i} M_1^*$	Monomer Initiation	Primary Radical
$M_n^* + M \xrightarrow{K_p} M_{n+1}^*$	Polymer Chain Propagation	Active Polymer Radical
$M_n^* + M_m^* \xrightarrow{K_t} M_d$	Chain Termination	(Dead) Polymer Chain
$M_n^* + O_2 \xrightarrow{K_o} M_d$ $R^* + O_2 \xrightarrow{K_o} R_d$	Oxygen Inhibition	Dead Polymer Chain Dead Radical

Table 2 – Ordinary differential equations corresponding to the dynamic concentration of the species inside the polymerization

Differential Equation	Specie Name
$\frac{\partial C_{in}}{\partial t} = -\frac{R_i}{2} - K_{self}C_{in}C_{R^*}$	Initiator
$\frac{\partial C_{R^*}}{\partial t} = R_i - K_p C_M C_{R^*} - 2K_t C_{M_n^*} C_{R^*} - 2K_t C_{R^*}^2 - K_o C_{O_2} C_{R^*}$	Free radical
$\frac{\partial C_M}{\partial t} = -K_p C_M C_{R^*} - K_p C_M C_{M_n^*}$	Monomer (double bond)
$\frac{\partial C_{M_n^*}}{\partial t} = K_p C_M C_{R^*} - 2K_t C_{M_n^*}^2 - 2K_t C_{M_n^*} C_{R^*} - K_o C_{O_2} C_{M_n^*}$	Chain-initiating polymer
$\frac{\partial C_{M_d}}{\partial t} = -K_t C_{M_n^*}^2 + 2K_t C_{M_n^*} C_{R^*} + K_o C_{O_2} C_{M_n^*}$	Dead chain (polymer)
$\frac{\partial C_{O_2}}{\partial t} = -K_o C_{O_2} C_{R^*} - K_o C_{O_2} C_{M_n^*} - D_{O_2} \left( \frac{\partial^2 C_{O_2}}{\partial x^2} + \frac{\partial^2 C_{O_2}}{\partial z^2} \right)$	Oxygen

Generally, the initiation rates can be very fast and are controlled by a combination of the source of radicals, light intensity, and temperature. Additionally, a self-dissociation rate of  $K_{self}$  is defined that acts to reduce the initiator concentration; it has its greatest impact when the concentration of free radicals is large.

To obtain a kinetic expression for the rate of polymerization, it is necessary to assume that  $K_p$  and  $K_t$  are independent of the size of the radical [14]. The rate of photochemical initiation  $R_i$  is given by

$$R_i = 2\varphi I_v \quad 1$$

where  $\varphi$  is referred to as the quantum yield for initiation and interpreted as the number of propagating chains initiated per light photon absorbed. The maximum value of  $\varphi$  is 1 for most photoinitiating systems.  $I_v$  is the volumetric photon absorption rate, called the volumetric intensity in this paper (refer to section 4). The factor of 2 in Eq. 1 is used to indicate that two radicals are produced per molecule undergoing photolysis.

Finally, the rate of polymerization  $R_p$  can be obtained from Eq.2 below [10,14]

$$R_p = K_p [M] \sqrt{R_i / 2K_t} \quad 2$$

where  $[M]$  is the concentration of monomer and  $K_p$  and  $K_t$  are the propagation and termination rates, respectively. It is seen that Eq.2 has the significant conclusion of the dependence of the polymerization rate on the square root of the initiation rate. Doubling the rate of initiation does not double the polymerization rate; the polymerization rate is increased only by the factor  $\sqrt{2}$ . This behavior is a consequence of the bimolecular termination reaction between radicals.

To calculate the initial concentration of initiator  $[In]_0$  and monomer double bond concentration  $[M]_0$ , the solvent density  $\rho$  ( $kg/m^3$ ) is required to convert the mass-based concentration ( $kg/m^3$ ) to molar-based ( $mol/m^3$ ). Considering a solution of n% (weight percent) of initiator where n is less than 5%, the volumetric change of solvent due to adding the initiator can be neglected. Hence, the total volume of solution can be considered as the total volume of solvent (Monomer). Therefore, the initial value of monomer concentration (double bond) is obtained

$$[M]_0 = n_{DB} \frac{\rho}{M_m} \quad 3$$

where  $\rho$  is the density of monomer,  $M_m$  is the molar mass (molecular weight) of monomer, and  $n_{DB}$  is the number of double bond(s) in a monomer. Note that based on acrylate type (mono or multi-functional) the number of double bonds should be considered in the above equation; for example, a tri-acrylate has three double bonds ( $n_{DB} = 3$ ). It shows that each monomer has three active components for polymerization.

In the same way, the initial concentration of the Initiator is calculated as follows

$$[In]_0 = \frac{n}{100 - n} \cdot \frac{\rho}{M_{in}} \quad 4$$

where n is the weight percent of initiator and  $M_{in}$  is the molar mass of initiator.

Finally, the simulation of the kinematic model provides a molar concentration of various chemical products in reactions. Consequently, the polymerization level, which is indicated by the degree of conversion (DoC), will be calculated at any arbitrary point simply by:

$$D_{conv} = \frac{[M_0] - [M_d]}{[M_0]} \quad 5$$

Once the resin reaches to a certain amount of  $D_{conv}$ , it is converted to gel and the viscosity of the solution increases sharply, corresponding to a rapid transition from a liquid state to a solid state. Therefore,  $D_{conv}$  provides a criterion for defining a boundary between liquid and solid states. Polymerization particularly in multifunctional monomer does not reach a complete conversion of reactants due to the sharp increase of viscosity as well as declining free volume. The ultimate  $D_{conv}$  can be measured by FTIR and is usually reported less than 0.7 in previous works. This restriction is also implemented in the proposed model. According to the knowledge of authors, limitation of

Using the rate constants for TMPTA+DMPA listed in Table 3, a conversion degree value of 0.23 was determined by fitting to the data obtained experimentally. The value of 23 percent is consistent with the value measured by Boddapati via micro-rheology[15]. The parameters used in this study, as well as previous studies, are summarized in Table 3.

### 3. Intensity Distribution Model

The illumination of light on a surface can be represented by an intensity distribution model. It will be used as an input of the volumetric intensity model which will be described in Section 4. The accuracy of the modeling depends on how well the predicted intensity profile matches the actual intensity. Two well-known approaches are available for this part – ray tracing method [16] and point spread function (SPF) [17]. The ray tracing approach is computationally intensive, while SPF may not incorporate the intrinsic non-uniformity of illumination in projection systems.

In this research, the SPF method, also known as super-Gaussian, was chosen as a high-performance solution for small patterns. It has been implemented based on research published by Emami et. al. [17]. The concept of approximating the intensity of a pixel by a Gaussian distribution has been elaborated also by other researchers [18,19].

Table 3- Estimated parameters of kinetic modeling for photopolymerization of TMPTA

Parameter (unit)	Description	Current Research		Boddapati [15]		Jariwala [7]
		with PB	w/o PB	with O <sub>2</sub>	w/o O <sub>2</sub>	
K <sub>p</sub> (m <sup>3</sup> /mol/s)	Propagation rate	0.26	0.26	0.26	1.61	1.66
K <sub>t</sub> (m <sup>3</sup> /mol/s)	Termination rate	0.39	0.39	0.39	14.34	1.31
K <sub>O</sub> (m <sup>3</sup> /mol/s)	Oxygen inhibition rate	2.2	1.8	2	-	125
K <sub>Self</sub> (m <sup>3</sup> /mol/s)	Initiator Self-Dissociation rate	1200	0	-	-	-
ε	Initiator molar absorption coefficient, decadic base	13	10	15	15	15
wt%	Initiator Concentration	2%	2%	5%	5%	5, 20%
DoC%	Criterion for solidified resin	23	23	20	20	20
I <sub>max</sub> (mW/cm <sup>2</sup> )	Maximum intensity	18.2	18.2	14	14	1.25

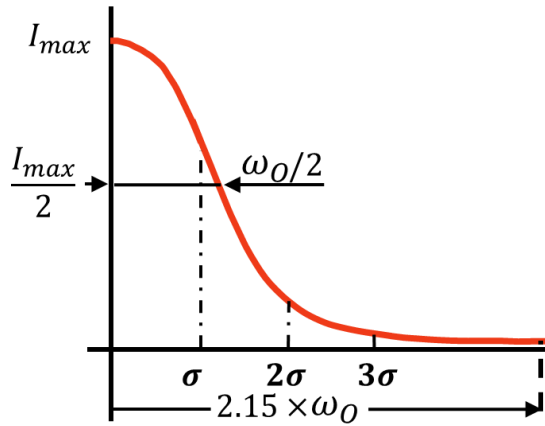


Figure 1- Gaussian Distribution of Intensity Profile,  $I_k(x)$ .

Based on the foregoing, the intensity distribution of a series of pixels on the image plane,  $I_s(x)$ , is given by Eq.6.

$$I_s(x) = \sum_{k=0}^n I_k(x) = \sum_{k=0}^n G_k I_{max} e^{-[4\sqrt{2\ln 2} (x-k\rho)/\omega_0]^2} \quad 6$$

where  $G_k$  is the grayscale level of the  $k$ th pixel (integer value between 0 to 255),  $I_{max}$  is the peak intensity of the full-on pixel,  $\rho$  is pixel pitch,  $\omega_0$  is Gaussian half width, and  $n$  is the total number of pixels. As shown in Figure 1,  $I_k(x)$  falls rapidly when moving away from the Gaussian origin, line  $x = 0$ . To increase the computing performance of the superposition calculation, an effective area (EA) is defined as the area receiving 99.99% of the total exposure [17]. This area is bounded by  $x = \pm 2.15\omega_0$ .

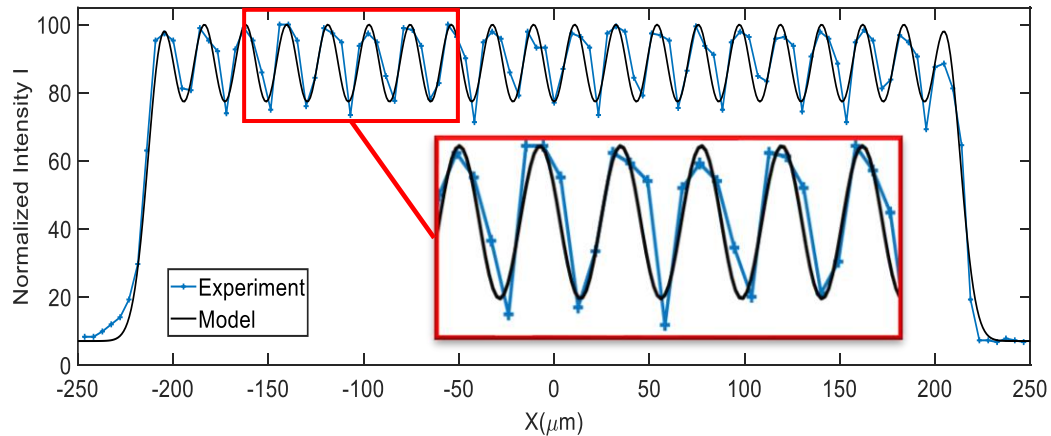


Figure 2- Normalized measured intensity profile vs. the super-Gaussian model for 20 pixels,  $I_s(x)$ .

A parameter identification method has been used to find the model's independent constants like as  $I_{max}$ ,  $\rho$  and  $\omega_0$ . The light engine employed in this research is capable of providing a wide range of intensities: 1-100 (mW/cm<sup>2</sup>).  $I_{max}$  is the average peak intensity of top-flat mask with Gray level of 255 (fully on mirrors) which is measured with a power meter.

The remaining parameters ( $\rho$  and  $\omega_0$ ) were tuned so that the model output fits the intensity profile measured by a CCD camera. A series of linewidths were chosen to show the generality of the model. The measured and calculated intensity distributions of a line pattern with a width of 100 pixels is shown in Figure 2. The intensity distribution of an irradiated mask composed of  $n$  pixels was calculated using Eq.6. Parameter optimization showed that the minimum discrepancy between the experiment and the model achieved when  $\omega_0=18.8 \mu\text{m}$  and  $\rho=21.6 \mu\text{m}$ .

#### 4. Volumetric Intensity

In physics, intensity is the power transferred per unit area, where the area is measured on the plane perpendicular to the direction of propagation of the energy. In photochemistry, any photon with sufficient energy can affect the chemical bonds of a chemical compound. Therefore, the intensity of absorbed light in moles of light quanta per volume per time, named volumetric intensity here, is required to calculate the number of affected bonds [10].

In some previous works, the expression given for initiation rate  $R_i$  (see Eq. 1) does not exhibit dimensional consistency [5,9,15,20]. For unit consistency, it is required that  $I_v$  has dimensions of moles per volume per time rather than an intensity (Einstein per unit area per time). The correct governing equations have been proposed in this section.

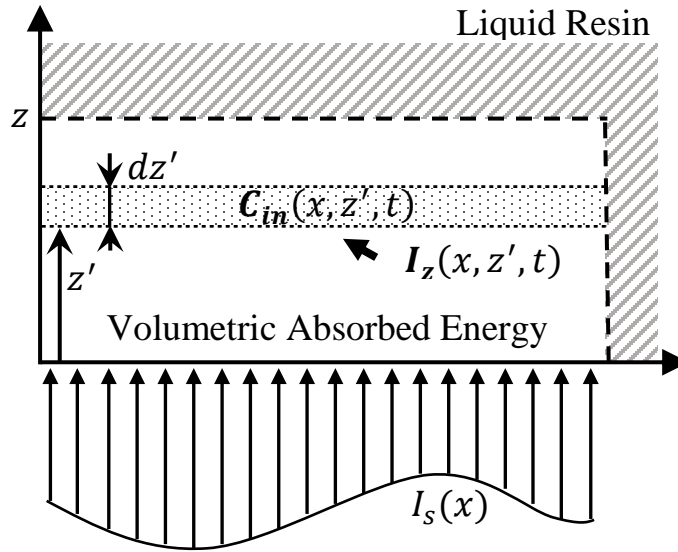


Figure 3- Volumetric Intensity  $I_v(x,z,t)$

The volumetric intensity  $I_v$  is based on the Beer–Lambert law. Figure 3 shows a schematic of the curing process in which the light distribution at the surface is  $I_s(x)$ . The light penetrates the resin and the light intensity declines to  $I(x, z)$  based on the Beer-Lambert law. Derivation of  $I_s(x)$  was described in Section 3. At a specific time,  $t$ , for any arbitrary infinitesimal layer  $dz$ , the concentration of absorber (initiator) is assumed to be constant in the  $z$  direction, or  $C_{in}(x, z, t) = C_{in}(x, z + dz, t)$ . In the other words, initiator concentration only varies along the  $x$ -axis.

For this study, the initiator is assumed to be the only UV absorber. Furthermore, the effect of light refraction can be neglected since the UV light is projected perpendicularly to the substrate. Also, the resin is optically clear before and after curing. Therefore, the light scattering effect is negligible.

In photopolymerization, the concentration of initiator  $C_{in}$  is uniform at the start, but it is not uniformly changed during the process. For each wavelength, the local light intensity  $I_z$  decreases along the beam direction  $z$  according to the integrated form of Beer's law [10,20]

$$I_z(x, z, t) = I_s(x, t) \cdot \exp \left[ -\alpha \int_0^z C_{in}(x, \acute{z}, t) d\acute{z} \right] \quad 7$$

where  $I_s$  is the incident light intensity at the outer surface of the reaction system and  $C_{in}(x,z,t)$  is the molar concentration of light-absorbing photoinitiator at the depth of  $z$  at time  $t$  in the reaction system. The absorption coefficient of initiator  $\alpha$  varies with wavelength and temperature. Here, the temperature variation is not considered. Although the initial concentration distribution of the initiator is uniform through the reaction region it will not remaining steady and uniform during the reaction. The integral expression in Eq. 7, corresponds to the variation of the initiator over the layer thickness. This spatial variation was not considered in some previous works or was averaged spatially [9,11,21]. Averaged concentration might be not accurate enough to demonstrate the PB effect.

The amount of absorbed light intensity at the distance of  $z$ ,  $I_a$ , is calculated as follows

$$I_a(x, z, t) = I_s(x, t) - I_z(x, z, t) \quad 8$$

The variation of  $I_v$  along the optical path direction,  $z$ , is obtained as the differential of  $I_a$  with respect to  $z$  as follows

$$I_v = \frac{\partial I_a}{\partial z} = -\frac{\partial I_z}{\partial z} = \alpha C_{in}(z) \cdot I_z \quad 9$$

To solve the above differential equation (Eq.9) and obtain  $I_z$ , the underneath boundary condition (BC) is considered. At the illuminated surface, and immediately above the substrate, the incident intensity is  $I_s(x, t)$ . We assume that at this surface neither reflection nor refraction is important. The BC at the incident light surface is defined by a Dirichlet BC,  $I(x, z = 0, t) = I_s(x, t)$ , which is a function of position ( $x$ ) and time ( $t$ ). Having a time-dependent intensity function adds the capability to simulate multiple masks during the illumination. The COMSOL ODE solver is employed to solve the volumetric intensity coupled to the rest of physics. Consequently, the attenuation of light changes during the illumination according to the concentration variation of photoinitiator.

The molar absorptivity  $\epsilon$ , formerly called the extinction coefficient, is often used instead of  $\alpha$ . It is related by  $\alpha = \epsilon \cdot \ln(10) = 2.3\epsilon$  and result from the use of the Napierian instead of the decadic base, respectively, in the Beer-Lambert law. The value of  $\epsilon$  used in this simulation was reported in Table 3. The energy in a mole of light (Einstein) is calculated by  $Nh\nu$  or  $Nhc/\lambda$  where  $h$  is Planck's constant,  $c$  is the speed of light,  $\lambda$  is the wavelength and  $N$  is Avogadro's number [14]. Thus, the Eq.9 can be rewritten as follows

$$I_v = 2.3\epsilon \cdot \frac{\lambda}{Nhc} \cdot C_{in}(z) I_z \quad 10$$

Here, the units of  $I_v$  and  $I_z$  are ( $mol \cdot m^{-3} \cdot s^{-1}$ ) and ( $W/m^2$ ) respectively. Thus, the difference between  $I_v$  and  $I_0$  can be large for thick sections.

## 5. Experimental Setup

Trimethylolpropane triacrylate (TMPTA), a trifunctional monomer with a technical grade containing 600 ppm of monomethyl ether hydroquinone (as an inhibitor), and 2,2-Dimethoxy-2-phenyl acetophenone (abbreviation - DMPA, trade name - Irgacure® 651) as a photoinitiator (Sigma-Aldrich) were used without further processing or purification. The weight ratio between the monomer and the photoinitiator was 98:2. The UV-curable resin was prepared by mixing these two compounds together and storing for one day until the initiator species was completely dissolved.

In this research, a high-performance UV light engine (LE) from VISITECH was employed to illuminate high resolution and uniform grayscale patterns. The system specification is summarized in Table 4. This LE has an adjustable optical system designed that enables variable magnification with the capability of reducing or enlarging the projected image from the DMD. For the current research, a magnification ratio of 2:1 has been selected. Furthermore, the high frame rate of 19 KHz reduces the minimum achievable exposure time to the order of 100  $\mu$ s. In the other words, it increases the vertical resolution (in direction of z-axis) for higher intensities.

Table 4- Specification of UV Light Engine

Specification	Value
DMD resolution	1920 $\times$ 1080 pixels
DMD type	0,95" 1080p UV Enhanced
Micromirror size	10.8 $\times$ 10.8 ( $\mu$ m <sup>2</sup> )
Pixel size (Image Plane)	21.6 ( $\mu$ m)
Light source	High Power LED
Light source wavelength	365 (nm)
Light source power	1 - 100 (mW/cm <sup>2</sup> )
Contrast ratio	Typical 1300:1 (full ON/full OFF)
Max binary frame rate	19.5 (KHz)

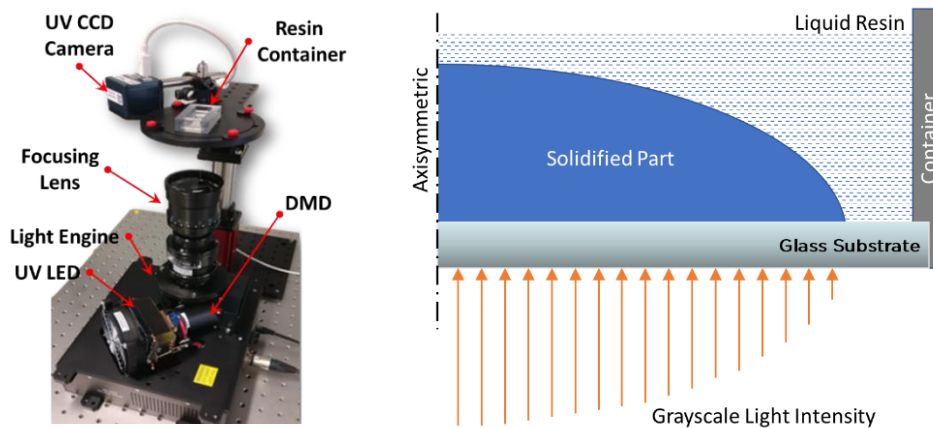


Figure 4- Experimental setup consists of a high-performance light engine, UV Camera, and Polymerization vat.

The experimental setup is shown in Figure 4, along with a schematic of grayscale irradiation of the resin bath through the glass substrate.

## 6. Results and Discussion

To illustrate the performance of the PB model, a comparison between the working curve with and without the PB effect is shown in Figure 5. The simulation result considering the PB effect can estimate the actual working curve of the resin up to a curing depth of 1100 $\mu\text{m}$  (Figure 5.b). This height provides adequate flexibility to design micro-optic parts. Without that, the simulation working curve only covers the curing depth less than 400 $\mu\text{m}$ . The experimental working curve of TMPTA shows super-logarithmic behavior. The proposed method with consideration of self-dissociation of initiator also shows the same behavior. However, the conventional method exhibits a logarithmic behavior.

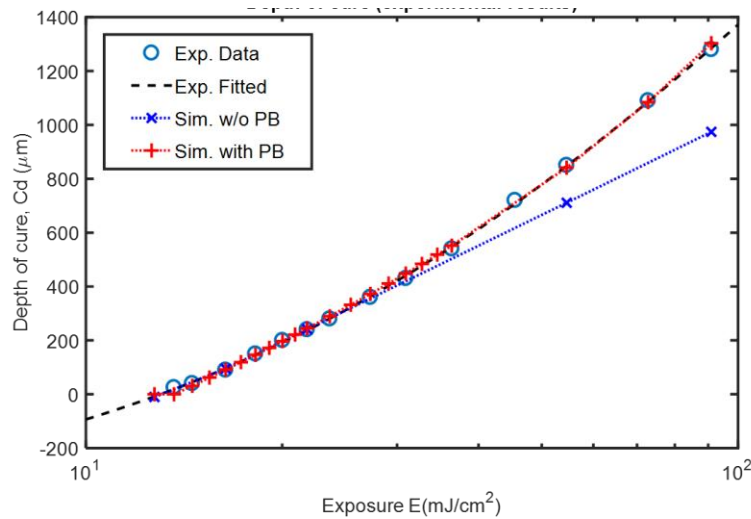


Figure 5- Comparison experimental working curve with simulation result without PB effect (blue dot line) and with PB effect (red dot line)

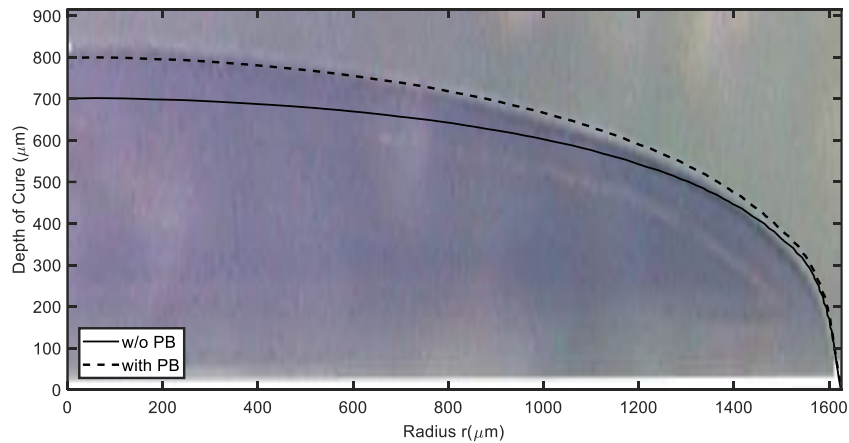


Figure 6- Side image of a fabricated aspherical lens with a radius of 1620 $\mu\text{m}$  and sag height of 800 $\mu\text{m}$ . Dash line and solid line represent the simulated profile with and without PB, respectively.

To study the feasibility of the proposed model for thick grayscale monolayer fabrication, an intensity profile was chosen to fabricate spherical lens with a sag height of 800  $\mu\text{m}$ . In parallel, this profile was imported into COMSOL and used as the input to predict the final cured profile with and without PB effect. Since the proposed model is an axisymmetric FEM simulation, only the cross-section of the fabricated lens is selected for comparison. The side image of the fabricated lens, as well as simulation results, are depicted in Figure 6. Although both simulated profiles demonstrate discrepancy, the error between the result with PB (dashed line) matches with the final experimental profile much better than the model without the PB effect.

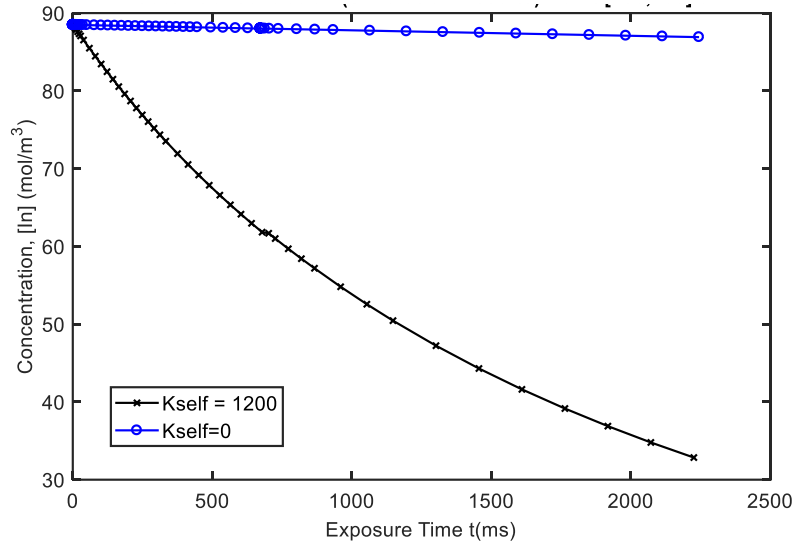


Figure 7- Simulation results of initiator concentration variation with PB ( $K_{self}=1200$ ) and without PB ( $K_{self}=0$ )

Figure 7 shows the consumption of initiator during UV exposure at the specific point of [100 $\mu\text{m}$ ,100 $\mu\text{m}$ ] in the simulated part shown in Figure 6 with and without the PB effect. A non-zero  $K_{self}$  value indicates that the PB effect is being modeled. Results demonstrate that the number of initiators consumed without the PB effect is very small compared to including the PB effect.

## 7. Conclusion

In this work, an improved multiphysics model of photopolymerization consisting of chemical reactions and UV irradiation has been demonstrated. In the chemical reaction part, the photobleaching effect has been simulated by considering a new self-dissociation reaction. A comparison between the simulated and actual working curve demonstrated considerable improvement in estimating depth of cure up to 1100  $\mu\text{m}$ . Furthermore, the proposed model capability was tested by fabrication of microlens with sag heights of 800  $\mu\text{m}$ .

Describing and utilizing a volumetric intensity instead of surface intensity provided a precise molar number of photons participating in the curing based on the surface intensity. It corrected the unit inconsistency shortcoming of the surface intensity that was observed in some previous works.

Future work will utilize the improved photopolymerization model in a process planning method to achieve high precision fabrication of optical components.

## 8. Acknowledgments

This research was supported by the Singapore National Research Foundation through the NAMIC program under fund no. 2016215. Any opinions, findings, and conclusions or recommendations expressed in this publication are those of the authors and do not necessarily reflect the views of the NAMIC.

## 9. References

- [1] X. Chen, W. Liu, B. Dong, J. Lee, H.O.T. Ware, H.F. Zhang, C. Sun, High-Speed 3D Printing of Millimeter-Size Customized Aspheric Imaging Lenses with Sub 7 nm Surface Roughness, *Adv. Mater.* 1705683 (2018) 1705683. doi:10.1002/adma.201705683.
- [2] P. Lehtinen, M. Kaivola, J. Partanen, Absorption cross-sections of Disperse Orange 13 and Irgacure 784 determined with mask projection vat photopolymerization, *Addit. Manuf.* 22 (2018) 286–289. doi:10.1016/j.addma.2018.05.006.
- [3] S. Huang, M. Li, L. Shen, J. Qiu, Y. Zhou, Fabrication of high quality aspheric microlens array by dose-modulated lithography and surface thermal reflow, *Opt. Laser Technol.* 100 (2018) 298–303. doi:10.1016/j.optlastec.2017.10.026.
- [4] F.C.M. van Kempen, Y. Hirai, F. van Keulen, O. Tabata, Automatic process design for 3D thick-film grayscale photolithography, in: 2013 Transducers Eurosensors XXVII 17th Int. Conf. Solid-State Sensors, Actuators Microsystems (TRANSDUCERS EUROSENSORS XXVII), IEEE, 2013: pp. 1625–1628. doi:10.1109/Transducers.2013.6627095.
- [5] J. Wu, Z. Zhao, C.M. Hamel, X. Mu, X. Kuang, Z. Guo, H.J. Qi, Evolution of material properties during free radical photopolymerization, *J. Mech. Phys. Solids.* 112 (2018) 25–49. doi:10.1016/j.jmps.2017.11.018.
- [6] A.S. Jariwala, F. Ding, A. Boddapati, V. Breedveld, M.A. Grover, C.L. Henderson, D.W. Rosen, Modeling effects of oxygen inhibition in mask-based stereolithography, *Rapid Prototyp. J.* 17 (2011) 168–175. doi:10.1108/13552541111124734.
- [7] A.S. Jariwala, Modeling and Process Planning for Exposure Controlled Projection Lithography (PhD diss.), Georgia Institute of Technology, 2013.
- [8] G.A. Miller, L. Gou, V. Narayanan, A.B. Scranton, Modeling of photobleaching for the photoinitiation of thick polymerization systems, *J. Polym. Sci. Part A Polym. Chem.* 40 (2002) 793–808. doi:10.1002/pola.10162.
- [9] K. Taki, Y. Watanabe, T. Tanabe, H. Ito, M. Ohshima, Oxygen concentration and conversion distributions in a layer-by-layer UV-cured film used as a simplified model of a 3D UV inkjet printing system, *Chem. Eng. Sci.* 158 (2017) 569–579. doi:10.1016/j.ces.2016.10.050.
- [10] G. Terrones, A.J. Pearlstein, Effects of optical attenuation and consumption of a photobleaching initiator on local initiation rates in photopolymerizations, *Macromolecules.* 34 (2001) 3195–3204. doi:10.1021/ma001235y.
- [11] D. Dendukuri, P. Panda, R. Haghgoie, J.M. Kim, T.A. Hatton, P.S. Doyle, Modeling of Oxygen-Inhibited Free Radical Photopolymerization in a PDMS Microfluidic Device, *Macromolecules.* 41 (2008) 8547–8556. doi:10.1021/ma801219w.
- [12] P.F. Jacobs, Fundamentals of stereolithography, in: *Int. Solid Free. Fabr. Symp.*, 1992.
- [13] V. Mucci, C. Vallo, Efficiency of 2,2-dimethoxy-2-phenylacetophenone for the photopolymerization of methacrylate monomers in thick sections, *J. Appl. Polym. Sci.* 123

- (2012) 418–425. doi:10.1002/app.34473.
- [14] G. Odian, Principles of Polymerization, John Wiley & Sons, Inc., Hoboken, NJ, USA, 2004. doi:10.1002/047147875X.
- [15] A. Boddapati, Modeling Cure Depth During Photopolymerization of Multifunctional Acrylates (MSc. Thesis), Georgia Institute of Technology, 2010. [https://smartech.gatech.edu/bitstream/handle/1853/33934/Boddapati\\_Aparna\\_201005\\_mast.pdf](https://smartech.gatech.edu/bitstream/handle/1853/33934/Boddapati_Aparna_201005_mast.pdf).
- [16] A.S. Limaye, D.W. Rosen, Process planning method for mask projection micro-stereolithography, Rapid Prototyp. J. 13 (2007) 76–84. doi:10.1108/13552540710736759.
- [17] M.M. Emami, F. Barazandeh, F. Yaghmaie, An analytical model for scanning-projection based stereolithography, J. Mater. Process. Tech. 219 (2015) 17–27. doi:10.1016/j.jmatprotec.2014.12.001.
- [18] H.-W. Kang, J.H. Park, D.-W. Cho, A pixel based solidification model for projection based stereolithography technology, Sensors Actuators A Phys. 178 (2012) 223–229. doi:10.1016/j.sna.2012.01.016.
- [19] X. Li, Y. Chen, Micro-scale feature fabrication using immersed surface accumulation, J. Manuf. Process. 45 (2017). doi:10.1016/j.jmapro.2017.04.022.
- [20] H. Peng, G. Chen, M. Ni, Y. Yan, J. Zhuang, V.A.L. Roy, R.K.Y. Li, X. Xie, Classical photopolymerization kinetics, exceptional gelation, and improved diffraction efficiency and driving voltage in scaffolding morphological H-PDLCs afforded using a photoinitiator, Polym. Chem. 6 (2015) 8259–8269. doi:10.1039/C5PY01414J.
- [21] M. Shusteff, A.E.M. Browar, B.E. Kelly, J. Henriksson, T.H. Weisgraber, R.M. Panas, N.X. Fang, C.M. Spadaccini, One-step volumetric additive manufacturing of complex polymer structures, Sci. Adv. 3 (2017) eaao5496. doi:10.1126/sciadv.aao5496.